

# Wave climate variability of Taiwan waters

Hwa Chien · Hao-Yuan Cheng · Ming-Da Chiou

Received: 21 April 2013 / Revised: 26 November 2013 / Accepted: 8 January 2014 / Published online: 28 January 2014  
© The Oceanographic Society of Japan and Springer Japan 2014

**Abstract** Global sea surface wind field data derived from NCEP reanalysis were used in driving a SWAN wave model to reconstruct historical wave records from 1948 to 2008. The reconstructed wave data were compared and verified by the observation of the data buoys of the Central Weather Bureau and the Water Resources Agency, Taiwan, and the National Data Buoy Center/National Oceanic and Atmospheric Administration, United States. Over the past six decades, the wave climate in Taiwan waters has undergone considerable changes. The annual mean significant wave heights have reduced an average of 0.31 cm/year. Winter wave heights have gradually dropped 0.86 cm/year, which are related to the weakening of winter monsoons. Regarding the inter-annual wave climate variation, the influence of El Niño/southern oscillation was substantial; the wave heights increased in La Niña years and decreased in El Niño years. In the past 60 years, extreme wave events have been concentrated in two periods: 1967–1974 and 2000–2008. More severe extreme wave events occurred in the latter compared with the former, and all were induced by typhoons. A clear trend, in which the summer (winter) extreme wave events have increased (decreased) gradually, has been identified. The 1980s was the transition period. After the transition period,

the annual occurrence of extreme wave events caused by typhoons exceeded those caused by an intense outbreak of winter cold surges, although the total number of the annual extreme wave events has not changed substantially.

**Keywords** Wave climate variability · Taiwan waters · ENSO · Numerical wave modeling · Empirical mode decomposition

## 1 Introduction

Recent studies have indicated that the frequency and intensity of extreme events triggered by global climate change are increasing (Easterling 2000; Parmesan and Yohe 2003; Barnett et al. 2006). The coastal zones, which are inhabited by high-density populations, are highly sensitive to extreme events because they are affected by both natural and human activities. The episodic short-term fluctuations in extreme events directly impact the social-economic stability in coastal areas because they disrupt the balance of the coastline as well as the ecosystem by altering the processes involved in the fluxes between the atmosphere and the ocean and the land and the sea. Some studies have shown that the transient effects of extreme events can induce substantial change of coastal and estuarine environments, causing severe coastal hazards including coastal erosion, inundations, harmful algal blooms, and coastal hypoxia (Zhang et al. 2004; Ringuet and Mackenzie 2005; Slott et al. 2006).

Wave climate refers to the long-term characteristics of ocean surface gravity waves. The surface gravity wave parameters used for statistics include significant wave height, period, wave direction, steepness, and wave spectral shape. These parameters reflect the fundamental exchange of energy and momentum at the ocean–atmosphere interface. In

H. Chien (✉) · H.-Y. Cheng  
Institute of Hydrological and Oceanic Sciences, National Central University, 300 Jhong-da Rd, Jhongli, Taoyuan 320, Taiwan  
e-mail: hchien@ncu.edu.tw

H.-Y. Cheng  
e-mail: hadawolf@gmail.com

M.-D. Chiou  
Institute of Oceanography, National Taiwan University,  
No.1 Sec.4, Roosevelt Rd., Taipei 106, Taiwan  
e-mail: mdchiou@gmail.com

addition to describing the change of the average mode of wave statistics, wave climate variation also reveals changes in the magnitude and frequency of extreme events on large temporal scales (Grabemann and Weisse 2008; Mori et al. 2010). Because the design of offshore platforms and coastal structures is determined by the loads of the largest wave height anticipated during a fixed design period, increases in the extremes of wave height events could shorten the lifespan of these structures. Coastal erosion is another critical issue; more than 80 % of beaches in Taiwan are currently eroding. The equilibrium condition of a coastal beach profile depends on seasonal or annual wave height, period, and direction. Moreover, climate systems and ocean-borne commerce are sensitive to sea surface conditions. Changes in wave climate have extremely large influences on ocean ecology, navigation, coastal protection measures, and ocean energy conversion (Harrison and Wallace 2005).

Because of the dense population and increasing intensity of industrial activities in the coastal zones of Taiwan, the wave climate change in Taiwan waters must be understood. However, detailed wave climate characteristics in the waters around Taiwan have not been explored in the existing literature. Taiwan is located at the western boundary of the North Pacific; therefore, in the following paragraphs, previous studies related to the wave climate changes in the North Pacific Ocean are reviewed.

Allan and Komar (2000) used in situ data measured from six data buoys in the North Pacific and suggested that the significant wave height in winter increased by 0.88 m from 1976 to 2000 because of the increasing occurrence of giant waves during hurricanes. A correlation analysis between wave height trends and the East Pacific index, Pacific Ocean oscillation index, and El Niño/southern oscillation (ENSO) showed significant correlations. Allan and Komar (2001) collected wave buoy data for coastal areas along the northwestern coast of the United States (states of Washington and Oregon) between 1978 and 2001, determining that violent storms led to increasing trends in wave height and more coastal hazards during the approximately 20-year period. During winter (October–March), significant wave height increased at a rate of 3.2 cm/year. Moreover, since 1976, when the National Data Buoy Center (NDBC)/National Oceanic and Atmospheric Administration (NOAA) buoy observation began, the occurrence probability of hazardous waves (significant wave height >6 m, duration longer than 9 h) on the western coast of the United States (northwest Pacific) increased. By using the NDBC buoy data from 1981 to 2003, Bromirski et al. (2005) suggested that the wave energy variability in the northeast Pacific is closely related to broad-scale atmospheric circulation modes that affect climate variability across the North Pacific and North America. Menéndez et al. (2008) also discussed the

variability of extreme wave height in the northeast Pacific based on field measurements from 26 buoys for 23 years (1985–2007). Their results showed a significant positive long-term trend in extreme wave height near the western US coast, which indicated that the extreme wave height increased at the rate of 2.35 cm/year. Menendez et al. also demonstrated the impact of El Niño on extreme wave heights. Aside from the buoy measurement, Gulev and Grigorieva (2006) analyzed the 45-year data obtained from a voluntary observing ship (VOS) (1958–2002) and showed a secular increase of winter wave height in both North Atlantic and North Pacific mid-latitudes of approximately 1.0–4.0 cm/year. Recently, Ruggiero et al. (2010) suggested that the significant wave height in the northwest Pacific has increased at a rate of approximately 1.5 cm/year since the mid-1970s, whereas averages of the five highest wave heights per year have increased at the greater rate of 7.1 cm/year.

By implementing numerical simulations, Graham and Diaz (2001) used reanalysis data published by the NCEP/NCAR to define cyclone data, compiling statistics of winter (December–March) cyclones in the northeast Pacific for the previous 50 years; the authors also used the dataset from NOAA buoys 46011 (34.9°N, 120.9°W), 46006 (40.9°N, 137.5°W), and 51001 (23.4°N, 162.3°W) to obtain significant wave height measurements. The Wave-watch III wave model was implemented to estimate the historical significant wave heights, and 50 years of wave data with a resolution of 1.5° latitude and 2° longitude were reconstructed. The frequency and strength of winter cyclones in the North Pacific, as well as the surface wind speeds at 25°–40°N, increased. There were considerable changes in the circumfluence around the Alaskan Bay. According to a comparison of the extreme values in observation data from the 1980s with the significant wave height from modeling data, increases in the extreme values of significant wave height were related to increases in wind speed as well as decreases in air pressure.

Concerning the northwest Pacific, Sasaki et al. (2005) studied changes in wave climate caused by storms in the waters around Sagami Bay between 1980 and 2003 by using buoys at 35°18'07"N, 139°20'56"E; storm data was obtained from the Regional Specialized Meteorological Center (RSMC), which is located in Tokyo and associated with the World Meteorological organization, WMO. The author performed an annual change analysis of significant wave height for summer and winter. First, the magnitude of significant wave height in summer (June–August) was related to typhoon activities; by contrast, the magnitude of significant wave heights in winter (December–February) was dominated by the strength of southerly winds in extratropical cyclones. Their results also showed that inter-annual changes in wave climate were subject to the impact

of storm activity. Sasaki and Hibiya (2007) analyzed ERA-40 wave field data published by the European Center for Medium-Range Weather Forecasts, ECMWF and wave data obtained from Objective Interpolation TOPEX/Poseidon (OITP). The authors applied empirical orthogonal function (EOF) analysis and linear regression models to significant wave height to estimate the average monthly wave height for every summer (June–August) in the northwest Pacific ( $20^{\circ}\text{S}$ – $40^{\circ}\text{N}$ ,  $90^{\circ}\text{W}$ – $120^{\circ}\text{E}$ ). The results showed that the wave height increased at the rate of 4 cm/year. The increasing trends were related to cyclonic circulation in the northwest Pacific. This cyclonic circulation was subject to the impact of warm sea surface temperature anomalies (Niño-3.4). The authors used average meridional wind anomalies in the area ( $5^{\circ}$ – $15^{\circ}\text{N}$ ,  $130^{\circ}$ – $130^{\circ}\text{E}$ ) as the principal component predictor, showing that the results of both sets of wave height were highly similar according to regression models.

Yamaguchi and Hatada (2003) adopted the shallow water wave model to calculate significant wave height in the waters around Korea. The resolution of this model in the area of the northwest Pacific was 5 km, reaching 0.5 km in the coastal waters of Korea. Because the authors used high terrain resolution, their study yielded more favorable results for the coastlines than did WAM 3G. Reanalysis data released by the ECMWF (1979–1998) and by the NCEP/NCAR (1948–1998) were used for wind field data and validated using observation results from two stations. The results showed that using two sets of wind fields to drive wave fields produced highly consistent results with observations concerning the changes in the wave climate around Korea. The authors then used 51 years of wave data 1948–1998 to perform trend analysis, determining that significant wave height exhibited an increasing trend in the first 10 years (1948–1957), and a weakly decreasing or no trend in the following 41 years (1958–1998).

Based on the aforementioned literature, reports of increasing significant wave height in the North Pacific are consistent. Wave conditions in coastal oceans are closely related to regional weather systems, indicating that the ongoing global climate changes directly impact the local wave climate (Sasaki et al. 2005). The coast of Taiwan experiences multiple typhoons every summer and severe monsoons every winter. Whether changes occur in wave climate, as well as the trends, severities, and the rate of changes, are issues that must be considered in policy decision making and design related to ocean resource use and coastal hazard mitigation. In order to provide knowledge and insight to the decision makers in Taiwan concerning the mitigation of coastal hazards related to global climate change, the purpose of this study was to clarify the dependency of coastal hazards on global climate change indexes. In addition, statistical analysis of extreme large

wave events was performed to provide a reference for risk analysis of ocean resource use. The present work is arranged as follows. In Sect. 2, the reconstruction of historic wave fields is described. The spatial and temporal variation of the wave climate is discussed in Sect. 3. The occurrence probability of extreme wave events is discussed in Sect. 4. The conclusions and potential research topics are provided in Sect. 5.

## 2 Reconstruction and validation of historical wave data

### 2.1 Model setup and the driving wind field

In this study, the SWAN wave model was used to hindcast the historical waves in the northwestern Pacific. To drive the wave fields, two main sources of reanalysis wind fields are currently available in the public domain, the NCEP/NCAR (NRA-40) and ECMWF global reanalyses. For climatological study, long-term and complete datasets are preferable. The NCEP/NCAR reanalysis data were used to drive a wave model of the northwest Pacific between 1948 and 2008. The wind fields were provided every 6 h at UTC00, 06, 12, and 18 with a spatial resolution of  $2.5^{\circ}$  longitude and  $2.5^{\circ}$  latitude. To obtain hourly wave data, the reanalysis wind fields were interpolated and downsampled to one-tenth of a degree by using a downscaling method proposed by Chiou et al. (2007). The computation domain of the SWAN, which is illustrated in Fig. 1, covered the area from  $5^{\circ}$  to  $35^{\circ}\text{N}$  and  $110^{\circ}$  to  $160^{\circ}\text{E}$ . The spatial resolution of the computational mesh was one-tenth of a degree. The computational temporal interval was 30 min. The resolution of the spectral domain was 0.04–1.0 Hz divided into 34 bands, and the directional resolution was  $11.25^{\circ}$ . The bathymetric data used in this study was the ETOPO2 database of the National Oceanic and Atmospheric Administration (NOAA)/National Geophysical Data Center (NGDC), and the mesh spacing was 2 min. In Fig. 1, the red dots on the coast of Taiwan indicate the locations of the Longdong data buoy ( $25.079^{\circ}\text{N}$ ,  $121.92^{\circ}\text{E}$ ) and Hualian data buoy ( $24.036^{\circ}\text{N}$ ,  $121.63^{\circ}\text{E}$ ). These two buoys, deployed at 30 m of water depth, several hundred meters from the shoreline, belong to the coastal ocean monitoring network that was established in 1998 and is operated by the Central Weather Bureau (CWB) of Taiwan. The red dot offshore indicates the location of NOAA/NDBC data buoy #52200 ( $144.79^{\circ}\text{E}$ ,  $13.35^{\circ}\text{N}$ ).

The anemometers of the data buoy were installed on a steel tripod approximately 3 m above sea level. The observed wind speed was corrected to U10 by using a neutral drag coefficient according to Large and Pond (1981). The comparison between the NCEP/NCAR wind fields and the correct U10 are illustrated in Fig. 2a and b,

**Fig. 1** The computation domain of present study. The red dots on the coast of Taiwan indicate the locations of Longdong data buoy ( $25.079^{\circ}\text{N}$ ,  $121.92^{\circ}\text{E}$ ) and Hualian data buoy ( $24.036^{\circ}\text{N}$ ,  $121.63^{\circ}\text{E}$ ). The red dot offshore indicates the location of NOAA/NDBC data buoy #52200 ( $13.35^{\circ}\text{N}$ ,  $144.79^{\circ}\text{E}$ )

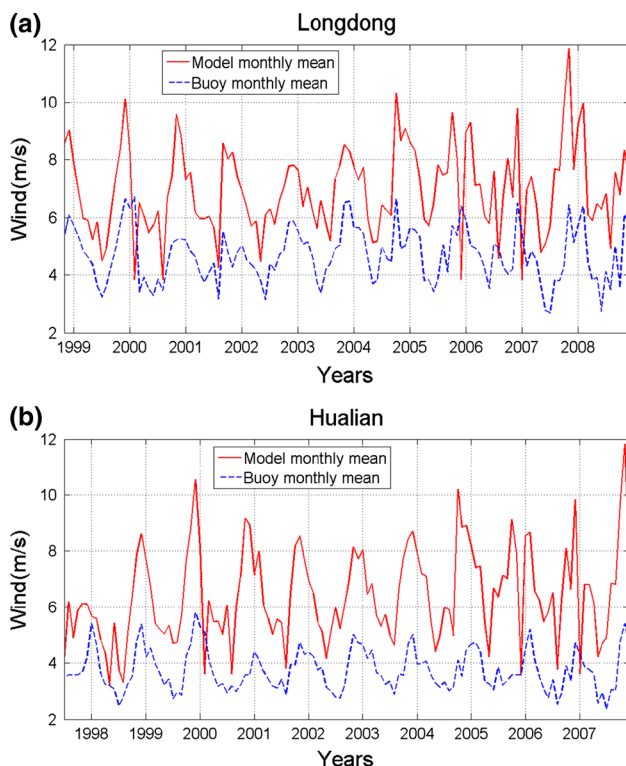
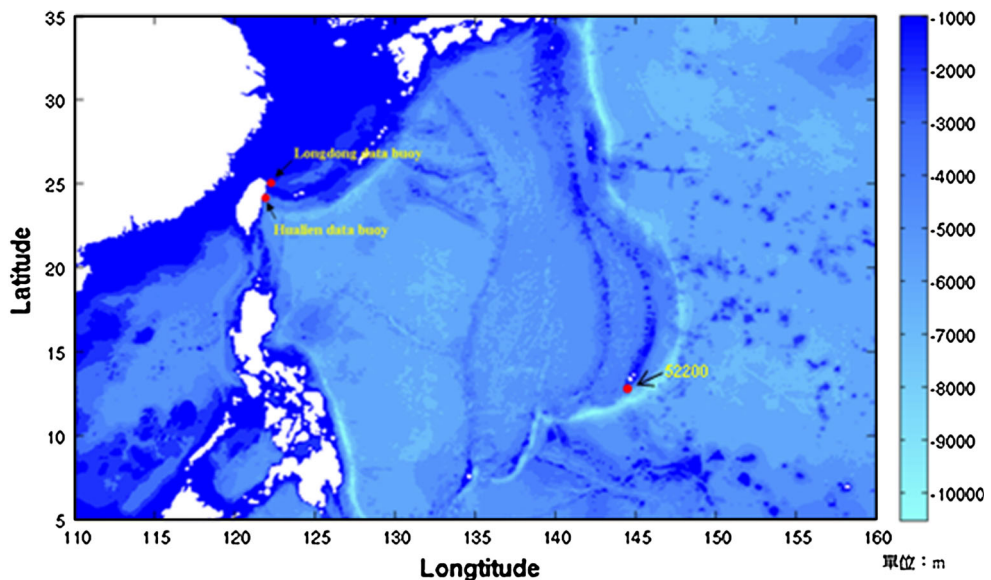


**Fig. 2** The comparisons of monthly averaged wind speed  $U_{10}$  between NCAR reanalysis fields, denoted by *dashed lines*, to the observations, denoted by *solid lines*, at **a** Longdong data buoy and **b** Hualian data buoy, respectively

which, respectively, represent the monthly averaged wind speeds observed from the Longdong and Hualian data buoys off the eastern coast of Taiwan. The monthly average of NCEP reanalysis wind data exhibits greater bias resulting from overestimating the  $U_{10}$  than does the observation from coastal buoys. However, this bias of

greater wind speed in the NRA-40 reanalysis dataset is not consistent with other studies. Yamaguchi and Hatada (2003) verified the same NCEP/NCAR and ECMWF reanalysis wind datasets in Korea Strait and Tsushima Strait. They found that neither of the wind datasets indicated lower speeds than did the observations. One possible explanation of the inconsistency between the NCEP/NCAR dataset and the measurements of coastal data buoys is that the buoys in the near-shore zone experience drag by coastal mountains. The NCEP/NCAR reanalysis wind field is synoptic in scale and may not fully reflect the wind features at the surface layer, especially for those of coasts where the land effects are critical.

Swail and Cox (2000) evaluated the NCEP/NCAR NRA-40 surface wind dataset as the forcing to the third-generation wave model in the North Atlantic. They addressed its deficiencies in the wave hindcast during extratropical storms and hurricanes. The storm peak wave heights in extratropical storms were systematically underestimated at high sea states. This resulted from the underestimation of peak wind speeds in major jet-streak features propagated from intense extratropical cyclones. Second, the tropical cyclone wind fields were not only poorly resolved (as expected on a coarse global grid) but often did not display sufficient energy at the grid resolution of the NRA model. Nevertheless, the wave hindcast using NCEP/NCAR reanalysis wind datasets reasonably depict the mean wave climate, and the results may be used as estimates of the actual wave climate (Swail and Cox 2000). In this study, the computational domain excludes the effects caused by the NRA-40's underestimation of extratropical storms. To enhance the resolution of typhoons, a method for the temporal interpolation of the extreme events was adopted for downscaling (Chiou et al. 2007). The

pathway and evolution of typhoons was considered in this method; thus, the wind and pressure dynamics in time and space were recorded. It was assumed that the typhoon center migrates on a straight line between two points in time. In addition, a linear change of the wind velocities and atmospheric pressure relative to the center of the typhoon was assumed during that period. Because the location of the center and the magnitude of the adjacent wind and pressure field can be calculated, the evolution of the typhoon can be described at finer meshes in time.

The SWAN model used in this study was version 40.71, which contains the dissipation source term proposed by Komen et al. (1984) and Alves and Banner (2003) as well as the revised wave growth term proposed by Booij et al. (1996, 1999) and Snyder et al. (1981). The Alves and Banner (2003) dissipation source functions were adopted to obtain more consistent wave hindcasts with observations. The dissipation source term  $S_{ds}$  is expressed as

$$S_{ds}(k, \theta) = \gamma_{ds} \cdot S(k, \theta) \quad (1)$$

where  $S(k, \theta)$  is the directional wave spectrum,  $k$  is the wavenumber  $\frac{2\pi}{L}$ ,  $L$  is the wavelength, and  $\theta$  is the dominant wave direction. The term  $\gamma_{ds}$  is expressed as follows:

$$\gamma_{ds} = -C_{ds} \cdot \left[ \frac{B(k)}{B_r} \right]^{p/2} \left( E_{tot} k_p^2 \right)^m \left( \frac{k}{\bar{k}} \right)^n \quad (2)$$

where  $C_{ds}$  is a constant,  $E_{tot}$  is the wave energy, and  $\omega$  is the wave frequency. The saturation spectrum,  $B(k)$ , is expressed as follows:

$$B(k) = k^3 S(k) \quad (3)$$

$$S(k) = \int_{-\pi}^{\pi} S(k, \theta) d\theta \quad (4)$$

$$\begin{cases} p = \frac{p_0}{p_2} + \frac{p_0}{p_2} \tanh \left\langle 10 \left\{ \left[ \frac{B(k)}{B_r} \right]^{1/2} - 1 \right\} \right\rangle, & B(k) > B_r \\ p = 0, & B(k) < B_r \end{cases} \quad (5)$$

The settings of the knobs are shown as follows:

Knob	$C_{ds}$	$p_0$	$m$	$n$	$B_r$
Value	$1.2 \times 10^{-3}$	4.0	0.3	1	0.002

The implementation of this wave model setting in the domain of Taiwan waters, driven by the reanalysis wind fields from the mesoscale non-hydrostatic model released by the CWB, Taiwan, was described by Lee et al. (2010). To quantify the model skill, the authors used standard error

**Table 1** The error parameters of the hindcast significant wave height

Error indice	Scatter index	BIAS (m)	RMS (m)
CWB Longdong	0.8982	0.06	0.24
CWB Hualian	0.8044	0.23	0.38
NDBC 52200	0.8812	-0.19	0.3

metrics, namely mean bias ( $b$ ), root mean square error (RMSE), and scatter index (SI), for hourly data over 4 months. The RMSE of significant wave height was 0.455 m and was 1.35 s for wave periods. The model overestimated the significant wave height 0.13 m and underpredicted the wave period 0.7 s (Lee et al. 2010). The error metrics demonstrating the hindcast performance of the present model for coastal oceans were similar in magnitude compared to the statistics published by Chawla et al. (2012) and Sterl et al. (1998) (Table 1). The model with the aforementioned settings was considered to be accurate.

## 2.2 Modeled wave climate comparison

To assess the bias of the output of the present model driven by long-term NCEP/NCAR datasets, wave observations from the data buoys of the CWB, Taiwan, and the NOAA/NDBC data buoy were used. In situ data of the Longdong and Hualian stations were adopted as representative wave characteristics of the north and east coasts of Taiwan. The data used for wave model comparisons were 10-year observations from the Longdong data buoy (1 November–31 December 2008) and Hualian data buoy (1 July–31 December 2007) as well as 5-year data from the NDBC/NOAA 52200 offshore buoy (1 January 2005–31 December 2009).

The comparisons between the monthly averaged hindcasts to the observations from the Hualian buoy, the Longdong buoy, and the NDBC 52200 buoy are illustrated in Fig. 3a–c, indicating that the overall biases of significant wave height were 0.06, 0.23, and -0.19 m, respectively.

Further examination of these biases showed that errors were often greater in conjunction with the lower observation success rates of data buoys. Buoy measurement success rates are defined as: (the number of successful measurements/the number of measurements that should have taken place in each month)  $\times 100\%$ . Based on the measurement success rates of the Longdong and Hualian buoys, the error indexes increase when the success rates are low. The reason may be that the low measurement success rates occur mostly during severe sea states (i.e., the onset of cold surges in winter), which caused abnormalities in the data buoys. When there was a malfunction, some large waves were not recorded, producing gaps in data on large waves and reducing the average measured wave heights.

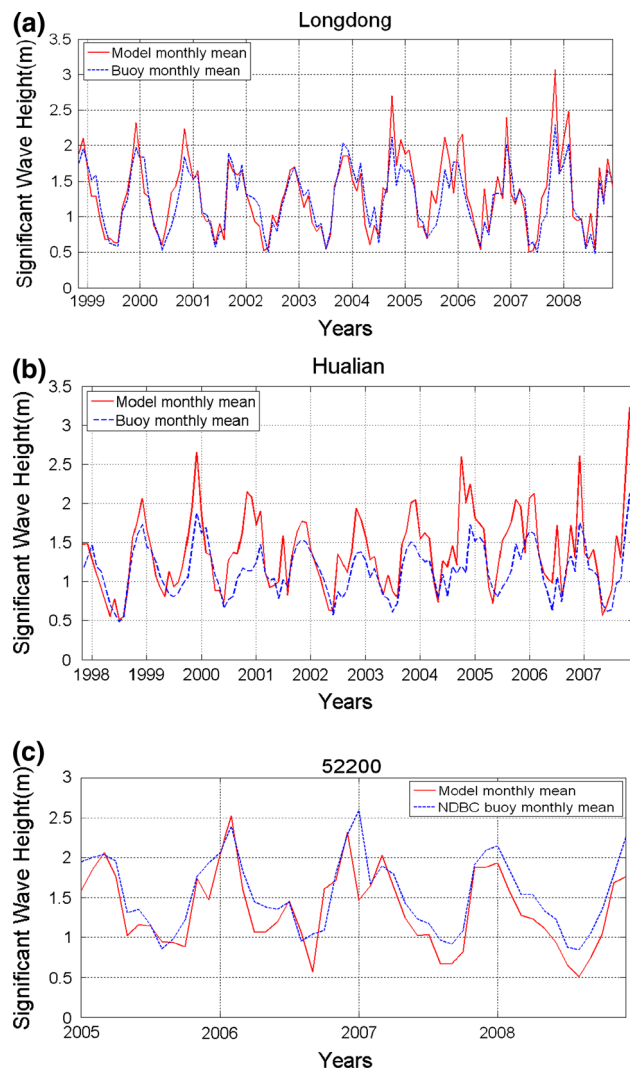


**Fig. 3** Comparisons of monthly averaged significant wave heights from model output and observations showing the field data from **a** the Longdong data buoy at the northeastern coast of Taiwan, **b** the Hualian data buoy at the eastern coast of Taiwan, and **c** the NDBC data buoy 52200

Therefore, significant wave heights calculated using the model were higher than the actual measured wave heights.

The same is true of the Longdong data buoy: when there were larger gaps between model-calculated significant wave height and measured wave height, as during November 2001, January and February 2006, January 2007, and February 2008, successful observation rates tended to be low.

### 3 Changes in wave climate around the coasts of Taiwan in time and space

The variations of wave parameters are a mixture of the response of the ocean surface to weather and climate

systems of various scales. This section presents an analysis of the wave climate variations in temporal and spatial domains to discern the long-term monotonic trend and the quasi-periodic oscillations, in which the long-term trend could be regarded as the influence of global warming. The appropriate partitioning of the quasi-periodic oscillations might allow us to narrate the relationship between the wave variations and the natural features of climate systems.

Among the traditional methods used for trend detection, numerous parametric and nonparametric methods have been developed. The Mann–Kendall test (Hirsch et al. 1982, 1984) is often applied in detecting the significance of a long-term monotonic trend in a time series (Lins and Slack 1999; Deser and Blackmon 1993). The magnitude of the trend, called the Mann–Kendall slope, is described linearly. The linear slope might be part of the oscillation of a greater period. Accordingly, a problem may arise regarding the data length required for detecting a possible trend from some transition points. By contrast, to identify the spatial and temporal oscillations in the dataset, singular spectrum analysis (SSA) and empirical orthogonal functions (EOF) are frequently used (Lee 2002; Wang and Swail 2001). Because SSA is the Fourier transform of EOF, when the Fourier transform is applied, each EOF component must be statistically stationary. However, a climate dataset is both non-linear and non-stationary.

Therefore, to overcome the difficulty of the nonlinear and non-stationary characteristics of climate datasets, a novel multi-timescale analysis method, ensemble empirical mode decomposition (EEMD; Wu and Huang 2009), was adopted in the present study. EEMD is an improved algorithm of empirical mode decomposition (EMD; Huang et al. 1998; Huang and Wu 2008) and has been proven to be quite versatile in a broad range of applications for non-linear and non-stationary data processes. EEMD is used to decompose original signals into multiple intrinsic mode functions (IMFs); it acts as a dyadic filter bank resembling the IMFs that represent the characteristics on different temporal scales (Flandrin et al. 2004). An IMF is not restricted to a narrow band signal, but can be both amplitude and frequency modulated. The remainders are residuals, which can be viewed as trends in the changes of original signals.

To define the IMFs in the original EMD, envelope calculations are used to determine the local maxima and minima separately (Huang and Wu 1998). Once the extrema are identified, all the local maxima and minima are connected by a cubic spline curve as the upper and lower envelopes. Their mean is designated as  $m_1$ , and the difference between the data and  $m_1$  is the first component,  $h_1$ :

$$h_1 = x(t) - m_1 \quad (6)$$

By repeating the process and replacing  $h_1$  with  $x(t)$ ,  $m_2$  is the mean envelope of  $h_1$ ,

$$h_2 = h_1 - m_2 \quad (7)$$

Each IMF,  $h_i$ , represents a simple oscillatory mode resulting from continuing the sifting process until the following conditions are met: the number of extrema is identical to the number of zero-crossings or, at most, differs by one.

$$x(t) = \sum_{i=1}^n h_i + r_n \quad (8)$$

where  $r_n$  is the residue, which can be either the monotonic trend or a constant. No more IMFs can be extracted from the residue.

The EMD method occasionally involves a mode mixing problem, which is defined as a single IMF including oscillations of dramatically disparate scales. Wu and Huang (2009) proposed EEMD to overcome the drawback by adding finite white noise to the data. They used the advantage of the statistical characteristics of white noise to perturb the signal and then cancel it out after it serves its purpose. The added white noise plays the role of filling in different scales of the original signal, and the noise can be cancelled out in the ensemble mean when enough trials are used in the process. Though EEMD adds different white noise to the data, the mean of IMFs of different cases in the procedure efficiently reduces the noise influence. Zhang et al. (2009) suggest that the number of ensemble trials should be approaching 100 to obtain robust result. This value is adopted in present study. The implementation steps for EEMD are described as follows (Wu and Huang 2009).

- (1) Add white noise to the data and apply EMD.
- (2) Subtract the same white noise used in Step (1) from the data, and apply EMD.
- (3) Stack the results of Steps (1) and (2).
- (4) Repeat Steps (1)–(3) several times, adding different white noise each time.
- (5) Stack all the IMFs of the same level and calculate the average.

The IMFs of different levels must occasionally be combined to obtain valid results with physical meaning. In this study, the IMF or a combination IMFs representing an oscillatory mode is considered to correspond to a certain climatological process. The amplitude of oscillation and frequency can change with time, but the mode does not produce riding waves and is not limited to narrowband signals.

### 3.1 Seasonal variations in wave climate

The time series diagrams for significant wave height, wave steepness, and dominant direction calculated at the northeastern coast (i.e., the location of the Longdong buoy) from

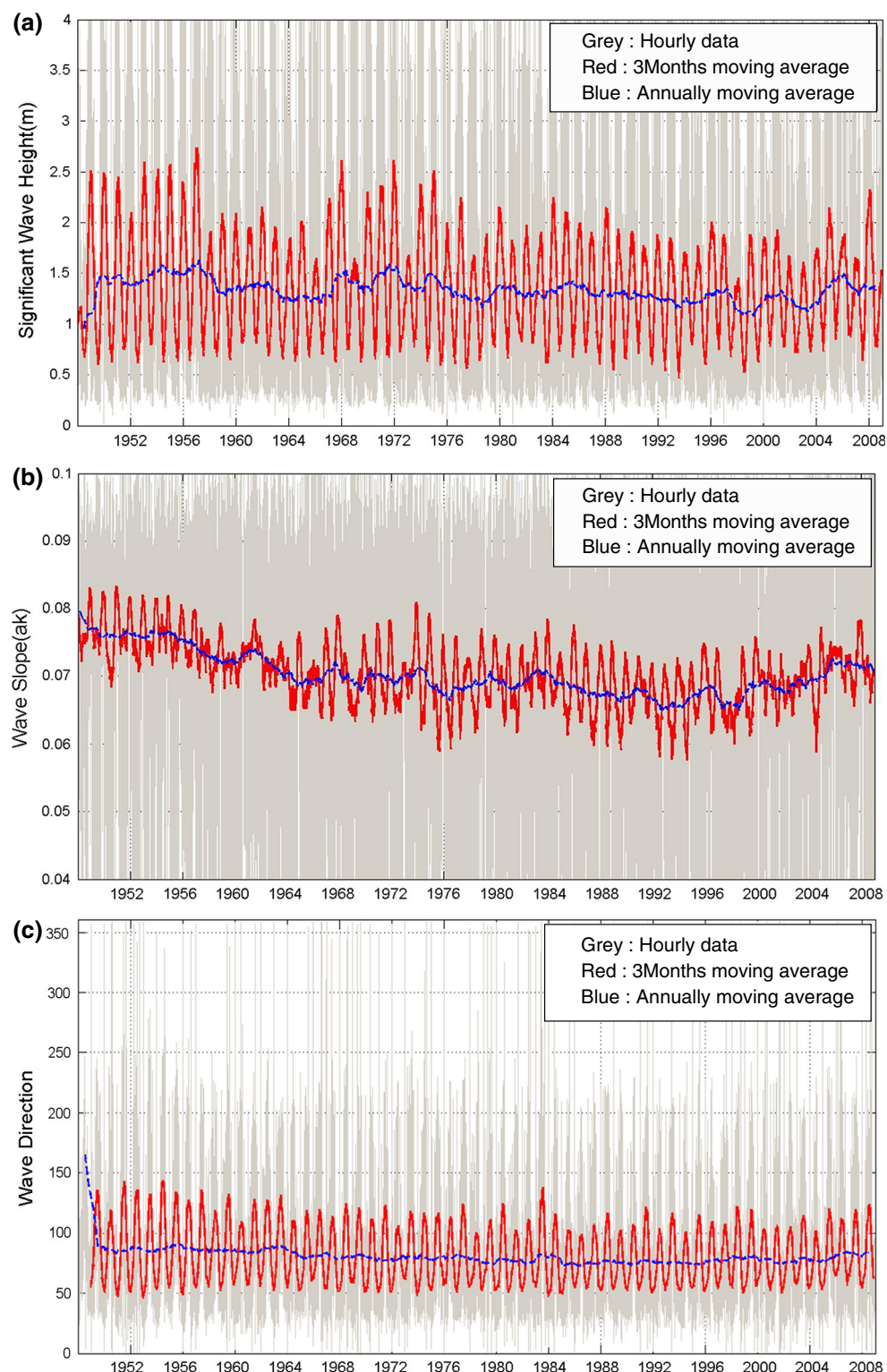
1948 to 2008 are shown in Fig. 4. Using the significant wave height ( $H_s$ ) at Longdong as an example, the gray lines represent the hourly data from the numerical model output. These hourly data are low-pass filtered using 3 months and an annually moving average to highlight the variations of the climatological time scale, as denoted by the red and blue curves, respectively, in Fig. 4.

To demonstrate the oscillations of various scales, the EEMD method was also implemented to the monthly run mean  $H_s$ . Eight IMF components and the residual components could be obtained accordingly, as illustrated in Fig. 5. The top panel is the monthly run mean  $H_s$ . The bottom panel is the residual component and could be regarded as the long-term trend. The Fourier analysis is applied to each IMF as shown in Fig. 6. The spectral peaks of the IMFs vary from 0.006 to 0.26 cycle/month. The corresponding peak periods of IMF1–IMF8 are 3.8 (IMF1), 11.9 (IMF2), 16.8 (IMF3), 28.4 (IMF4), 51.1 (IMF5), 127.8 mons (IMF6), 170.3 (IMF7), and 255.5 months (IMF8), respectively. With the aim of investigating the intra-annual variations, the IMF1 and IMF2 are superimposed to represent the seasonal oscillation, as their periods are within 12 months. The IMF1 + IMF2 can be regarded as the significant wave height anomaly. We compare the 3-month run mean of  $H_s$  to the IMF1 + IMF2 + residue, as illustrated in Fig. 7. The results for both the monthly moving averages and EEMD of wave height signals clearly exhibit the in-phase oscillations with a period of 12 months.

The wave height oscillations in Fig. 6 reached each local maxima in January and exhibited greater values than the overall mean during the winter months (NDJF) and smaller values than the mean during the summer season (JJAS). During the summer months, the wave heights were approximately 0.88, 1.01, and 0.58 m for the northeastern, eastern, and western coasts, respectively, whereas, during summer seasons, the  $H_s$  values were approximately 1.94, 1.91, and 1.18 m, respectively. The wave height, wave steepness, and wave direction at different data buoys during the winter and summer seasons are listed and compiled in Table 2, which shows that the winter wave energy contributes more than 85 % of the annual mean total energy, whereas the wave energy in summer is limited.

According to the EEMD results, at the Longdong data buoy, wave heights, and wave steepness in winter were 2.2 and 1.2 times higher than were those in summer, respectively. At the Hualian data buoy, wave heights differed by 1.9 times between the winter and summer seasons, and wave steepness differed by 1.3 times; at the Hsinchu data buoy, average wave heights differed by 2 times between the winter and summer seasons, and wave steepness differed by 1.2 times. This substantial ratio between winter and summer wave climates indicates the negative

**Fig. 4** Time series of hourly model output at Longdong (northeastern coast of Taiwan) and corresponding removing average over 2 months and 1 year. **a** The significant wave heights and **b** the wave slope in the Longdong area, northeastern coast of Taiwan. The gray lines denote the simulated hourly time series data. The red lines are the 2-month running average of the hourly data. Significant seasonal oscillations are obvious. The blue lines are the annual running average of hourly data. The inter-annual variation can be identified



influences on the capacity factor regarding the wave energy power conversion. As can be seen in Fig. 7, the estimation of this ratio would be underestimated if the seasonal variation signal is derived from moving average.

The differences in wave height between summer and winter might be a result of dominating Eastern Asia

monsoon systems (i.e. the North Pacific subtropical high in summer and Siberian high in winter). During the winter season, beginning in mid-September, the Mongolian region experiences high-pressure cold air masses and temperature drops. Air pressure is highest in January and February, and it later decreases because of rising temperatures in the

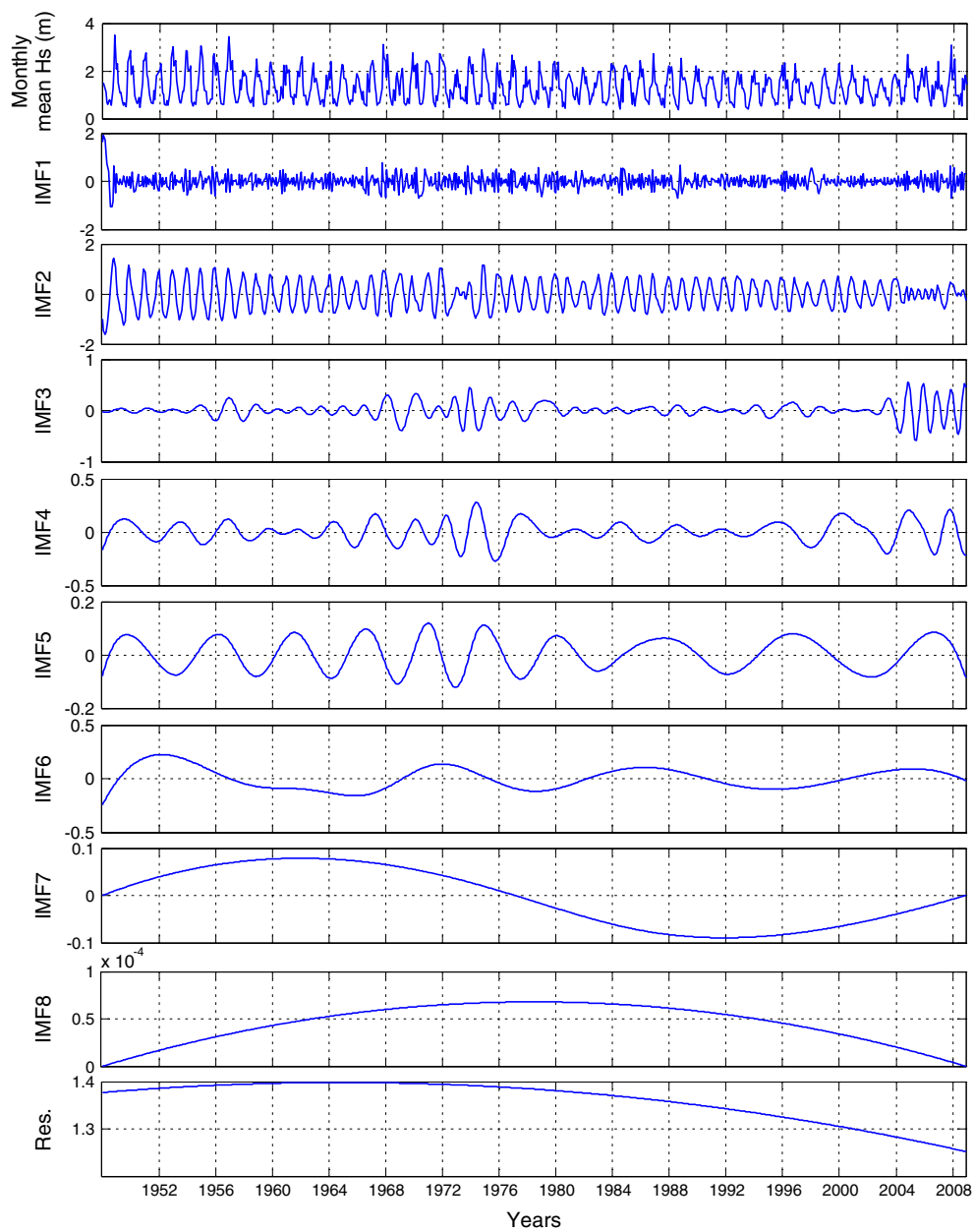


**Fig. 5** The intrinsic mode functions of significant wave height at Longdong. The *top panel* is the monthly mean significant wave height

northern hemisphere. By May, high-pressure cold air masses no longer impact the weather. Because high-pressure cold air masses primarily impact the temperature from October to April, prevailing winds move toward low-pressure areas and are influenced by Coriolis force. Winds that are directed northeast in areas south of South China and Taiwan are referred to as winter monsoons, which produce a primary impact on the weather systems and dry, cold climates.

Jan et al. (2002) analyzed the monthly mean wind stress vectors from 1986 to 1995 derived from a weather station in the Taiwan Strait. They showed that the northeast

monsoon begins in mid-September, peaks from October to January, and weakens continuously thereafter. By comparison, the southwest monsoon in June and July is considerably weaker. These prevailing monsoon systems provide the background environment for wave development.

The annual average significant wave heights of Longdong (northeastern coast), Hualian (eastern coast), and Hsinchu (western coast) are, respectively, 1.34, 1.37, and 0.83 m. The significant wave heights at the Hualian and Longdong data buoys are similar, with only small differences in average values. Average significant wave heights

**Fig. 6** The Fourier spectra of each IMF of Longdong significant wave heights

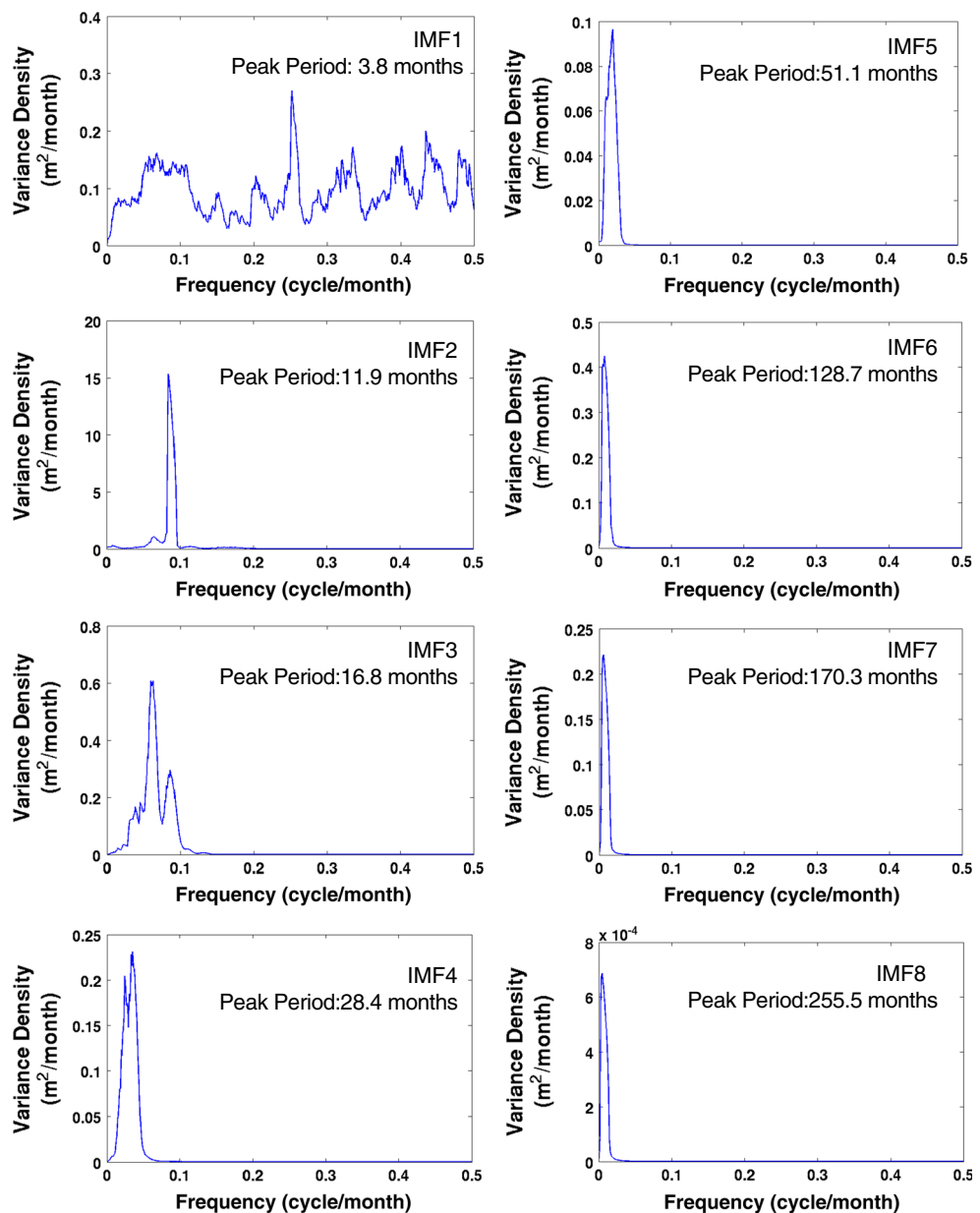


**Fig. 7** The comparison of the  $H_s$  time series obtained from the low-pass 3-month moving average of model output (solid blue) and the IMF1 + IMF2 + trend of monthly mean (dashed red)

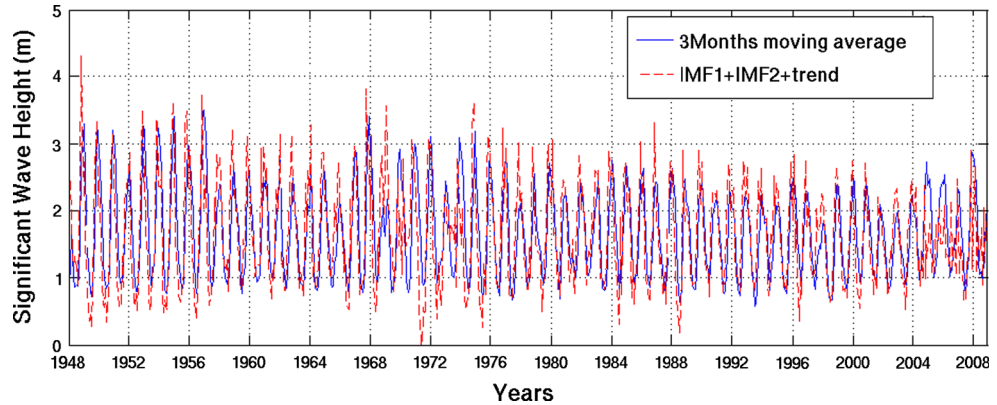


**Table 2** Average of wave parameters over 1948–2008

Location	Parameter	Summer average	Winter average	Annual average
Northeastern coast (Longdong)	Significant wave height (m)	0.88	1.94	1.34
	Wave energy (KW/m)	4.92	16.16	9.40
	Wave steepness (ak)	0.05	0.06	0.06
	Wave direction (°)	164	53	73
Eastern coast (Hualian)	Significant wave height (m)	1.01	1.91	1.37
	Wave energy (KW/m)	5.59	15.07	8.97
	Wave steepness (ak)	0.04	0.05	0.05
	Wave direction (°)	163	71	86
Western coast (Hsinchu)	Significant wave height (m)	0.58	1.18	0.83
	Wave energy (KW/m)	1.32	4.78	2.76
	Wave steepness (ak)	0.06	0.07	0.06
	Wave direction (°)	33	31	36

in Hsinchu are comparatively low, because the western coast is located by the Taiwan Strait and is therefore affected by limited fetch.

### 3.2 Dependency of interannual wave climate variations to ENSO

As shown in the previous section, the East Asia winter monsoon, accompanied by a strong Siberian high and active cold surge, is the dominating factor for the wave variation around Taiwan. Every winter, the shift of north-easterlies and the outbreak of cold surges influences the water volume transport through the Taiwan Strait and the continental shelf of the East China Sea (Jan et al. 2002), and exerts a strong impact on wave development and extreme wave events. Zhang et al. (1997) used NCEP/NCAR reanalysis data from 1979 to 1995 to analyze inter-annual variations in winter monsoons and established a link between the inter-annual variation of the winter monsoon and the cold surge with tropical atmospheric and oceanic phenomena. They demonstrated the high correlation between the East Asia winter monsoons and ENSO. Chen et al. (2001) examined the impact of inter-annual changes and determined that the strength of winter monsoons is subject to the impact of tropical Pacific SST anomalies. Their results indicated that, during the winter seasons of El Niño years, winter monsoons in East Asia appear to be weakened. According to north wind frequency analysis, frequencies tend to be lower in the areas around the East China Sea and the South China Sea during the winter

seasons of El Niño years; north wind strength is also considerably reduced.

Bjerknes (1969) suggested that El Niño and La Niña represent the interaction between the atmosphere and ocean of the tropical Pacific and that their occurrence is related to the strength or weakness of Walker circulation. El Niño and La Niña are coupled: the warm oceanic phase, El Niño, accompanies high air surface pressure in the western Pacific, whereas the cold phase, La Niña, accompanies low air surface pressure in the western Pacific. This interactive oscillation between the eastern and western regions of the equatorial Pacific is referred to as the Southern Oscillation. The El Niño/La Niña–Southern Oscillation could be identified according to the variations of the SST of the tropical eastern Pacific Ocean and the air surface pressure in the tropical western Pacific, which leads to the development of anomalously warm ocean water temperatures off the western coast of South America.

There are several indicators of the strength and phase of ENSO: the Southern Oscillation index (SOI) and multiple indicators developed by the NOAA in the Pacific Niño region. The SOI involves subtracting the observed air pressure in Darwin, Australia, from the observed air pressure in Tahiti. The expression representing the normalized difference is as follows:

$$\text{SOI} = \frac{\text{SLP}_{\text{Tahiti}} - \text{SLP}_{\text{Darwin}}}{\sigma} \quad (9)$$

$\sigma$ : standard deviation of air pressure difference when SOI is positive, La Niña occurs; when SOI is negative, El Niño occurs. Its magnitude indicates the strength.

Regarding the periods in which ENSO phenomena occur, Glantz (2001) suggested cycles of 2–7 years, typically lasting approximately 12–18 months, while McPhaden and Picaut (1990) suggested cycles of 2–10 years. McPhaden (1999) showed that the strongest El Niño year in the twentieth century was 1997–1998, in which many regions experienced severe disasters and losses; the global climate characteristics in that year were also different from those of normal years.

In this section, the dependency of wave height anomaly on the ENSO is investigated. The SOI from the Climate Prediction Center (CPC) of the National Ocean Atmospheric Association (NOAA) for the period from January 1948 to December 2008 was used as an indicator for determining the occurrence of El Niño and La Niña. Anomalies in significant wave height were determined based on cycles of ENSO occurrence (3–10 years) by using Eq. (10).

$$H_{\text{anomaly}} = \frac{\overline{H}_{s(\text{mean})} - \overline{H}_{s(\text{movingaverage})}}{S_{s(\text{movingstandard})}} \quad (10)$$

where,

$\bar{H}_{s(\text{mean})}$ : annual average significant wave height

$\bar{H}_{s(\text{movingaverage})}$ : annual moving average of significant wave height, where  $i$  is 3–10 years

$S_{i(\text{movingstandard})}$ : annual moving standard deviation of significant wave height, where  $i$  is 3–10 years.

The significant wave height anomalies were compared with the inter-annual variations that resulted from applying the EEMD method to the Longdong buoy data, as shown in Fig. 8. The periods correspond to the spectral peak of IMF3, IMF4, and IMF5 are 16.8, 28.4, and 51.1 months, respectively. The superposition of these modes represents the 2- to 10-year variations, as denoted by the green line. The EEMD results exhibit consistent oscillation patterns with the wave height anomalies, as shown by the red line.

Figure 8 indicates that, typically, a negative (positive) SOI represents an El Niño year (La Niña year), which corresponds to less pronounced (more pronounced) significant wave height anomalies. No phase delay could be identified between these two phenomena, but some abnormal wave height anomalies do not correspond to the annual average of the SOI. Regression analysis was performed between changes in the annual average of the SOI and the significant wave height from EEMD. The results exhibited a positive correlation between the sum of IMF3 to IMF5 to SOI with correlation coefficients of 0.476, indicating a moderate correlation.

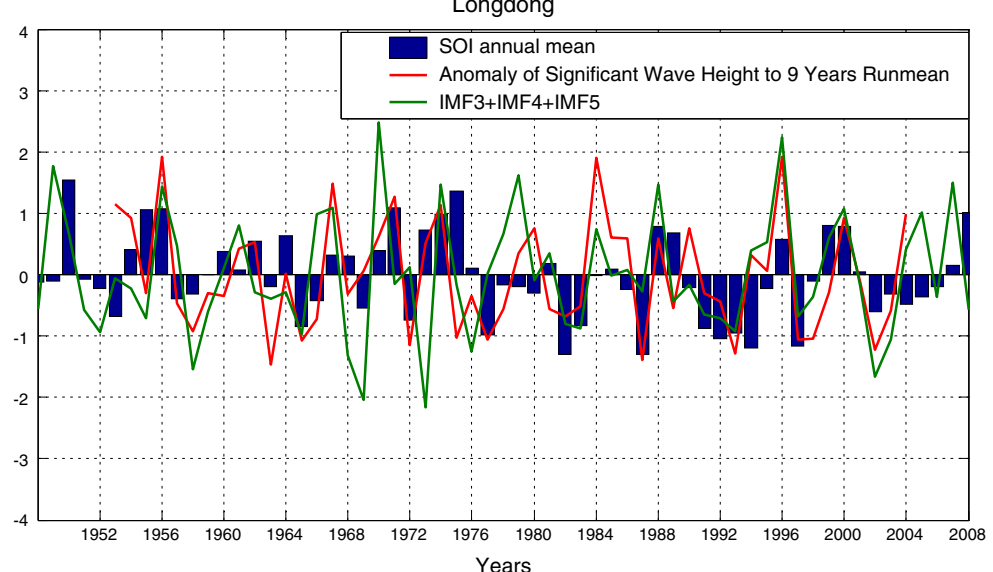
The variability of wave height and wave energy has been shown to depend on ENSO. Similarly, recent studies (Dodet et al. 2010; Wang and Swail 2001; Woof et al. 2002) on the wave climate variability in the Atlantic Ocean proposed that inter-annual fluctuations in wave height are controlled by the North Atlantic Oscillation (NAO). Dodet

et al. (2010) investigated the correlation between 57-year (1953–2009) hindcasted wave data and the Winter North Atlantic Oscillation index (WNAO) and discussed the wave data spatial variability. They revealed a strong positive correlation between the wave height and the WNAO index at northern latitudes and a significant negative correlation at southern latitudes. The results provide strong evidence of the link between the ocean and atmosphere climate dynamics, because the wave parameters were determined to be significantly related to the SOI or WNAO indexes.

ENSO variability has been strong in the past 30 years; ENSO phenomena occurred from 1982 to 1983, 1987 to 1988, 1991 to 1992, 1993, 1994 to 1995, 1997 to 1998, 2002 to 2003, 2004 to 2005, and 2006 to 2007 (Wang et al. 2000) at differing strengths. Moreover, strong La Niña phenomena occurred from 1975 to 1976, 1984 to 1985, 1988 to 1989, 1998 to 1999, and 2000 to 2001 (Wang et al. 2000), causing the SST in the eastern and central Pacific to be 1–2 °C lower than the climatological average. In addition, the La Niña phenomena which occurred from 1995 to 1996 and at the beginning of 2006 were comparatively weak.

Yeh et al. (2009) and Collins et al. (2010) suggested that, because of global warming, the mean climate of the Pacific region will likely undergo significant change. The year-to-year ENSO variability is controlled by the delicate balance between amplifying and damping feedback, and one or more of the physical processes that are responsible for determining the characteristics of ENSO will be modified by climate change. However, Collins et al. (2010) and Nicholls (2008) indicated that, because of the lack of evidence, whether the ENSO variability will be enhanced or reduced remains unknown.

**Fig. 8** The comparison of SOI annual mean (blue bar) to the significant wave height variations that estimates using EEMD (green line) and the anomaly to 9 years moving average (red line)



### 3.3 Wave climate changes across decadal periods

The inter-annual variations of wave climate and ENSO are not stationary, and can be modulated by the Pacific Decadal Oscillation (PDO). The PDO is a long-term El-Niño-like pattern of Pacific climate variability. It can be detected as warm or cool surface waters in the Pacific Ocean, north of 20°N. During a high phase, the west Pacific becomes cool and part of the eastern ocean warms; during a low phase, the opposite pattern occurs. It shifts phases on at least an inter-decadal time scale, usually approximately 20–30 years (Mantua and Hare 2002). Wang et al. (2008) investigated the interdecadal modulation of the PDO on the impact of the ENSO on the East Asian winter monsoon (EAWM). Their results showed that, when the PDO is in its low phase, ENSO exerts a strong impact on the EAWM. To examine changes across longer periods, we used EEMD to analyze long-term trends in wave climate in the northwest Pacific. The periods correspond to spectral peak of IMF6, IMF7, and IMF8 were greater than 10 years. To determine whether IMF6–IMF8 are associated with PDO, the PDO of 2-year moving averages were plotted in a time series diagram, as shown in Fig. 9. By summing IMF6–IMF8 following EEMD analysis, the periodic oscillation for at least 10-year periods was produced. Among the three components, shown in Fig. 5, IMF8 was O(3) magnitudes weaker than were IMF6 and IMF7. A correlation analysis indicated a moderate inverse correlation ( $r = -0.33$ ), demonstrating that the decadal oscillations of IMF6–IMF8 might be dependent on PDO.

### 3.4 Trends in wave climate changes from 1948 to 2008

In the case of the Longdong data buoy, wave heights have been trending downward for the past 60 years, as shown in

the bottom panel of Fig. 5. The wave heights slightly decreased from 1964 to 2008 at a rate of approximately 0.31 cm/year. We separated the summer (JJAS) and winter (NDJF) significant wave heights on an annual basis and obtained the time series of annual mean summer wave heights and mean winter wave heights. Then, the EEMD was applied to both time series to estimate the residues of both signals as illustrated in Fig. 10. It could be identified that wave heights in the summer season tended to increase annually, whereas winter season wave heights tended to decrease. Overall, wave height in the winter season exhibits a gradual downward trend, decreasing an average of 0.86 cm/year, and wave energy decreases of 0.2 kW/m/year. There also seems to be an increasing trend for wave height in summer seasons, in which wave height increases by an average of 0.5 cm/year and wave energy increases by 0.1 kW/m each year.

In addition to the temporal trend at Longdong, the spatial variation was addressed. The model output of the 60-year data was separated into a former 30-year subset and a latter 30-year subset. The subtractions of the average of the former subset from that of the latter, which represent the spatial distribution of long-term winter and summer wave climate changes, are shown in Fig. 11. Figure 11 indicates that summer season wave heights in the mid-latitude regions (17°–27°N) on the eastern side of Taiwan increase at a rate of 0.6–1.0 cm per year on average. Regarding the winter wave climate in the Luzon Strait and the region in the eastern waters of Taiwan, the wave height trends are decreasing at a rate of 0.4–1.0 cm per year on average.

These significant decreasing trends in winter coincide with the results of Gulev and Grigorieva (2006) regarding the eastern equatorial Pacific. Gulev and Grigorieva (2006)

**Fig. 9** The decadal significant wave height oscillations and the PDO index

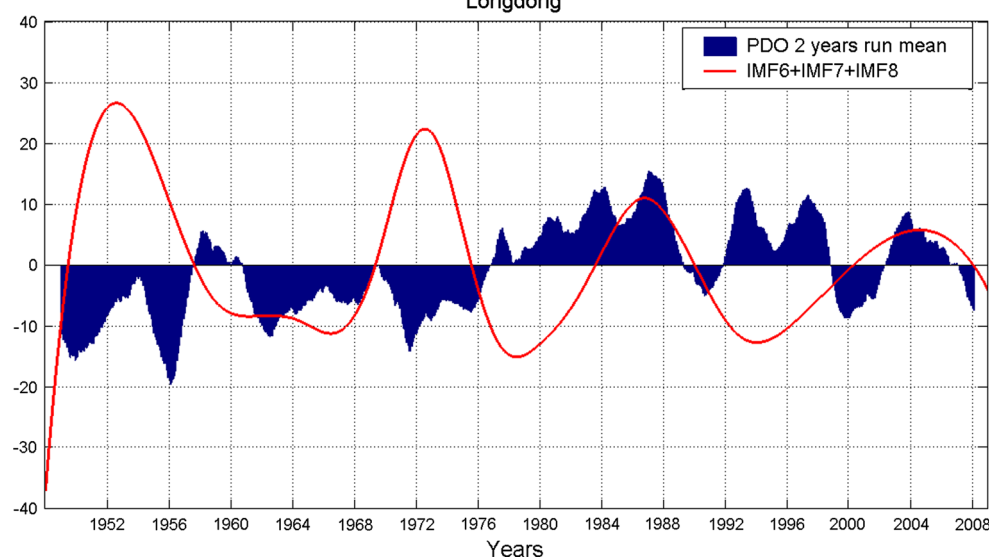


**Fig. 10** The long-term trends of significant wave heights in **a** the summer season and **b** the winter season

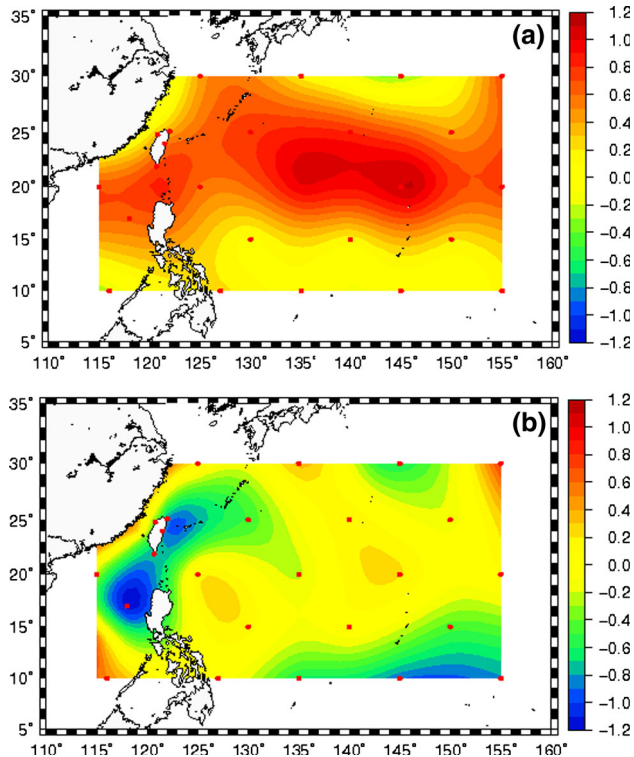
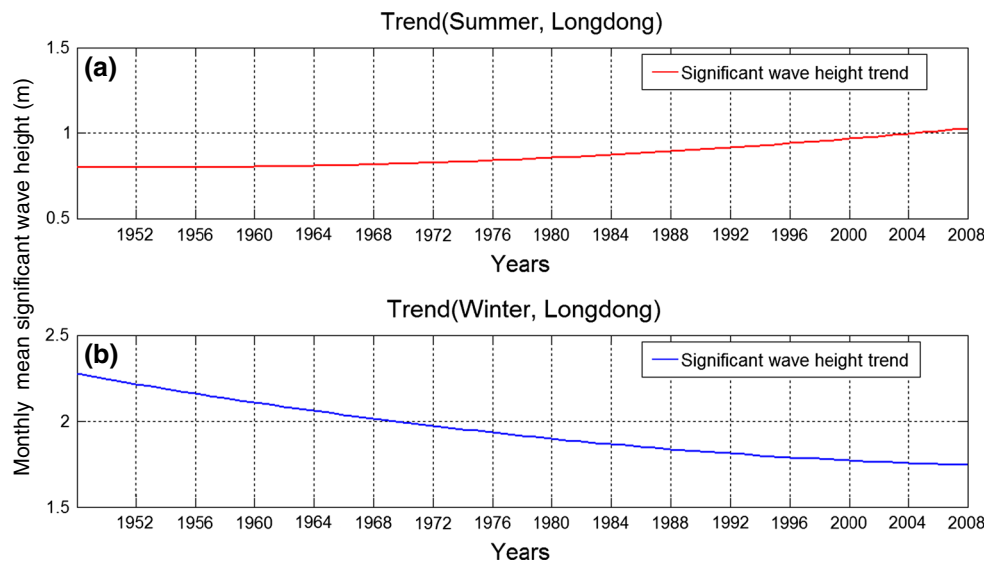


**Fig. 11** The spatial distribution of long-term trend of significant wave height in **a** summer and **b** winter. The unit of the colorbar is cm/year

analyzed VOS data from 1958 to 2002 and demonstrated an upward change of up to 1.4 cm/year in the annual mean Hs in the majority area of the North Pacific. A large area of growing wave height can be identified along the North Pacific mid-latitudinal storm track. The largest linear trend of change in wind sea exceeded 2.0 cm/year. Trends in the swell height were weaker and ranged from 1.0 to 1.5 cm/

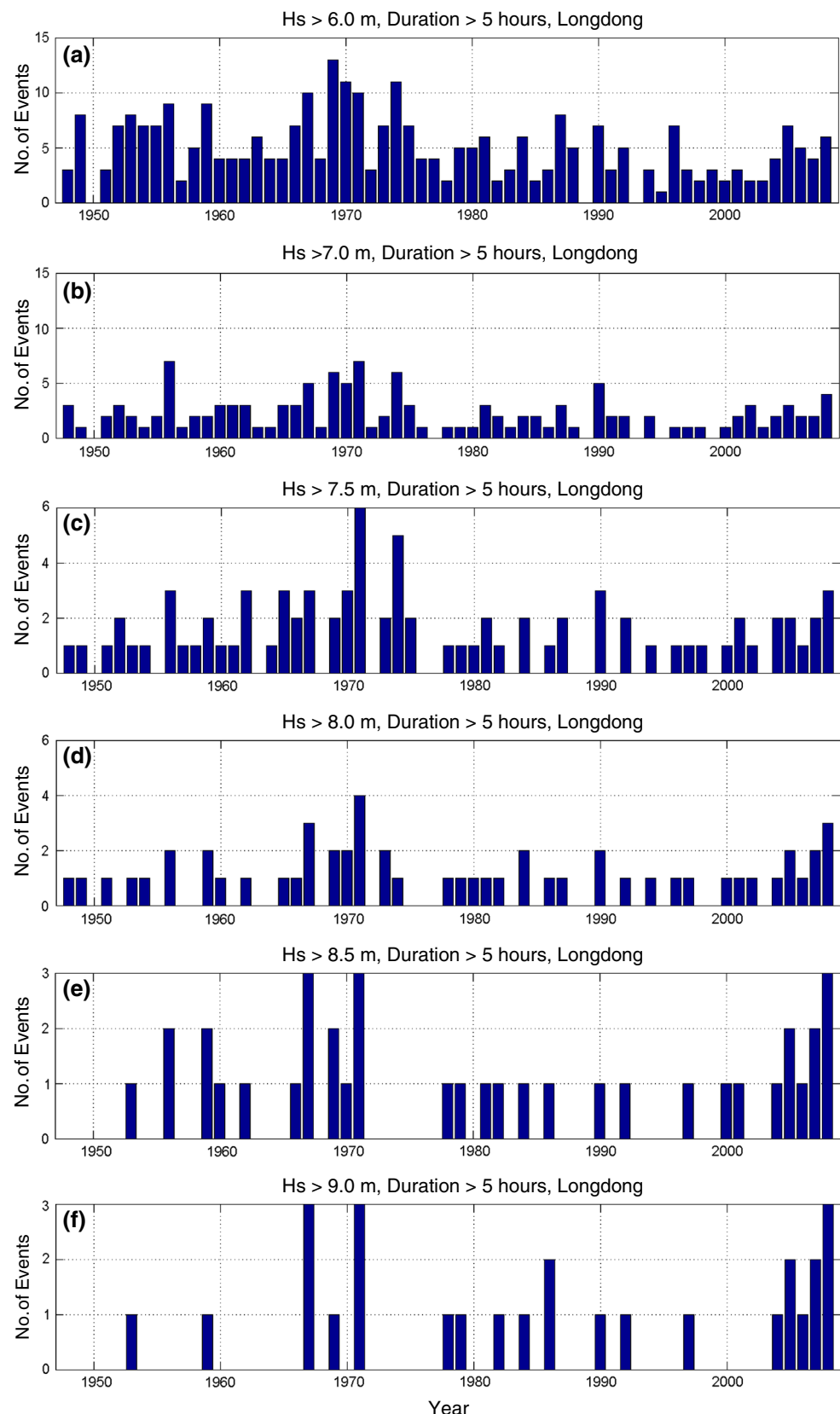
year. The behavior of wave climate variability is considerably different in the eastern and the western regions of the North Pacific. Gulev and Grigorieva (2006) indicated the significant negative trend in winter significant wave height, decreasing from 1.0 to 1.5 cm/year in the North Pacific eastern equatorial regions, and 0.5–1.5 cm/year in the vicinity of Taiwan waters. Our estimates are qualitatively consistent with those of Gulev and Grigorieva (2006).

#### 4 Occurrence probability of extremely large wave events

##### 4.1 Frequency analysis of extremely large wave events in the temporal domain

The waters around Taiwan have long experienced extreme wave events, delivering direct impacts to coastline erosion and destroying coastal infrastructure and impacting maritime safety (Vanem et al. 2012). In this study, an extremely large wave event (ELWE) is defined as an event involving significant wave heights greater than certain thresholds that occurs for longer than 5 h. Frequency analysis of the data at Longdong, Hualian, and Hsinchu was performed. The thresholds of significant wave heights were 3.2 m for Hsinchu (western coast) and 6.0 m for Longdong and Hualian (eastern coast). The numbers of occurrences of ELWEs meeting various conditions are depicted in bar graphs in Fig. 12a–f. The number of ELWEs decreases when the thresholds are tightened. According to panels a–c, the ELWEs were highly concentrated in the years 1956–1960, 1966–1975, and 2000–2008. Especially in the years close to 1970, the occurrence of ELWEs was more

**Fig. 12** The numbers of extreme wave events per year in the Longdong area. Extreme wave events are defined as **a**  $H_s > 6.0$  m and continue for  $>5$  h, **b**  $H_s > 7.0$  m and continue for  $>5$  h, **c**  $H_s > 7.5$  m and continue for  $>5$  h, **d**  $H_s > 8.0$  m and continue for  $>5$  h, **e**  $H_s > 8.5$  m and continue for  $>5$  h, and **f**  $H_s > 9.0$  m and continue for  $>5$  h



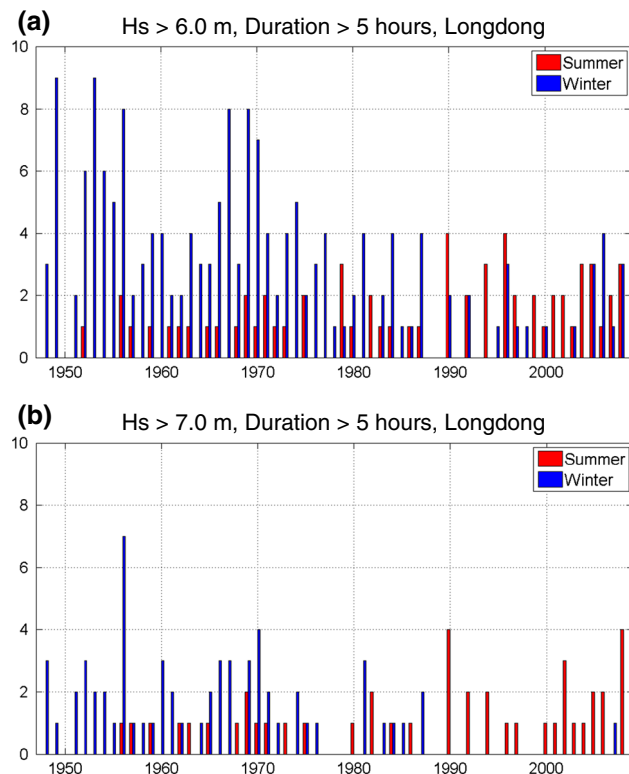


**Fig. 13** The number of extreme wave events per year. Extreme wave events are defined as **a**  $H_s > 6.0$  m and continue for at least 5 h, and **b**  $H_s > 7.0$  m and continue for at least 5 h. Red bars denote the events occurring during summer (June–September), blue bars represent the events occurring during winter (December–March). The trend of increasing/decreasing numbers of extreme events during summer/winter can be seen

than 10 annually when a threshold of  $H_s > 6$  m was applied. Consistent trends can be also found when using the Hualian and Hsinchu dataset. When tightening thresholds to  $H_s > 8$  m, a constant increase in ELWE occurrence from 2000 to 2008 can be identified, as shown in panels e and f. This result indicates that the recent ELWEs were more severe than those that occurred in the 1970s.

The frequencies of extreme events are further categorized based on the winter (NDJF) and summer (JJAS) seasons, as shown in Fig. 13; red indicates summer, whereas blue indicates winter. Figure 13a shows that ELWEs in which wave heights were greater than 6 m were relatively frequent in the winter seasons from 1950 to 1985. By contrast, ELWEs occurred much less frequently in summer during the same period. However, from the beginning of the 1980s, the occurrence of ELWE in summer began to increase. By contrast, the winter ELWEs gradually decreased in number and eventually reached their minimum in the late 1980s.

The winter ELWEs are associated with outbreaks of severe cold surges. There have been many efforts to understand and to predict the variation of the winter

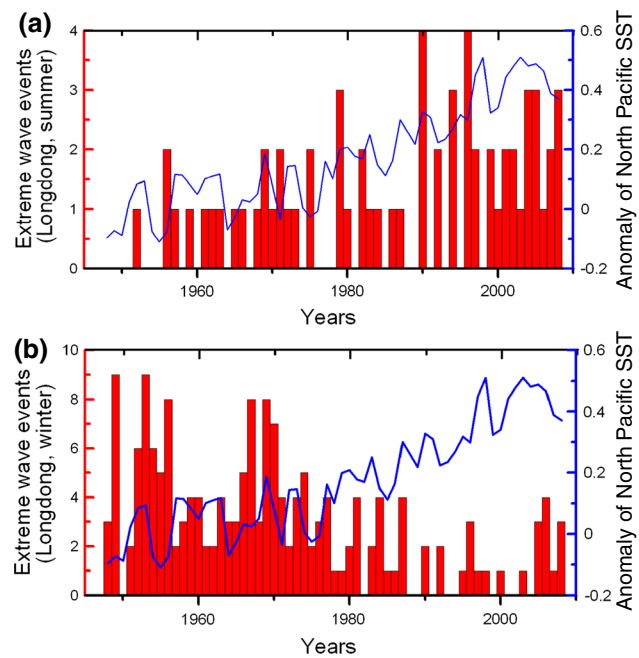


**Fig. 14** The number of extreme wave events at Longdong in **a** summer and **b** winter versus the Pacific surface temperature anomaly

monsoon in East Asia. Previous studies have shown that, in the past 50 years, the strength of the Siberian high/East Asia winter monsoon exhibits both intensive inter-annual oscillations and a decreasing trend (Gong and Wang 1999; Gong and Ho 2002; Chen et al. 2001; Kang et al. 2006). The East Asian monsoons not only control the local weather and climate in the East Asian region but also influence the convection and the SST near the Maritime Continent. Wang et al. (2000) noted the existence of a Pacific–East Asia teleconnection pattern caused by the positive thermodynamic feedback between the anticyclonic anomaly and the SST in the western North Pacific. Kitoh's (1988) results also indicate the impacts of the SST in the western North Pacific on the East Asian winter monsoon.

By using the western North Pacific SST as an index to describe the strength of winter monsoons, we plotted the annual occurrence of winter ELWEs and the annual western North Pacific SST anomaly, as shown in Fig. 14b. The red bar indicates the annual occurrence of winter ELWE at the Longdong coast, whereas the blue curve shows western North Pacific SST anomalies. Correlation analysis revealed that the correlation coefficient was  $-0.51$ , indicating that the frequency of ELWEs off the northeast coast of Taiwan during winter is inversely proportional to the SST; a higher SST is associated with fewer occurrences of extreme events. These results suggest that the number of winter ELWE variations is possibly correlated to the weakening of winter monsoons.

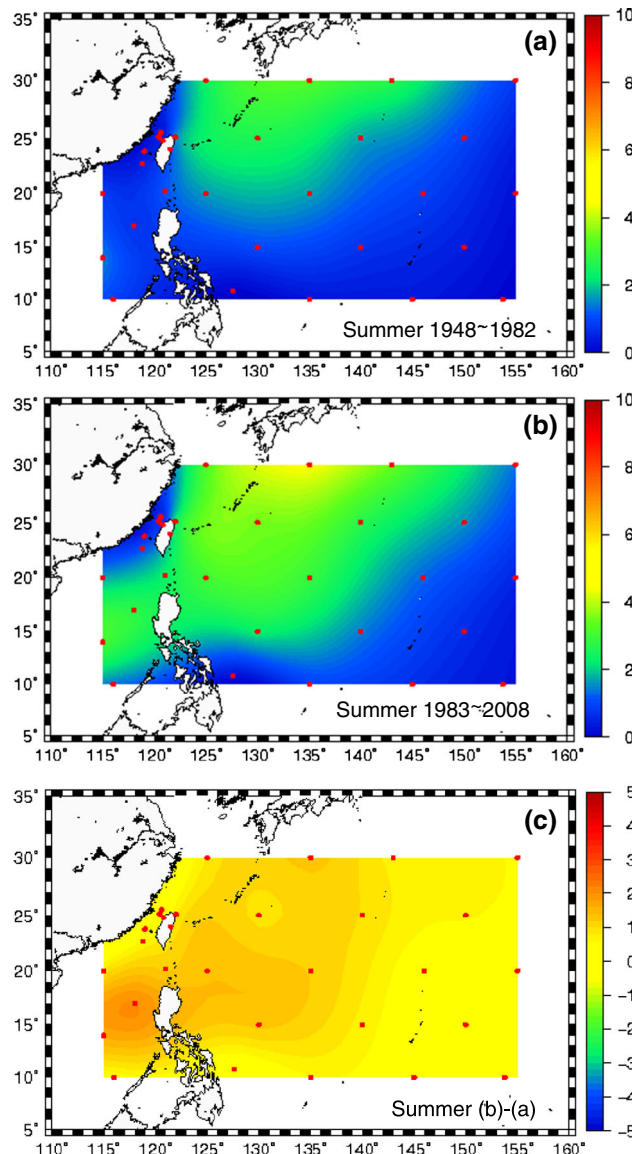


**Fig. 15** The spatial distribution of the annual extreme wave events in summer: **a** average from 1947 to 1982, **b** average from 1983 to 2008. The difference is illustrated in **(c)**

Concerning the summer ELWEs, the occurrence dates of the summer ELWEs were verified from the historical typhoon records from the CWB. The summer ELSEs coincided with the typhoons, without exceptions. Does the increasing occurrence of summer ELWEs reflect the trend of typhoon intensity variation in the western North Pacific?

An increasing trend in the SST of the western North Pacific and the North Pacific of approximately  $0.6^{\circ}\text{C}$  over the past 30 years was identified (Emanuel 2005). High-SST water provides the atmosphere in this region with abundant water vapor. Convergence occurs between the lower atmosphere and the easterlies near the tropical northwest Pacific, providing the low-level positive vorticity disturbances necessary for the development of typhoons.

Emanuel (2001) noted that increases in SST directly cause increases in the maximum potential intensity (MPI) of typhoons. In addition, Emanuel (2005) proposed the potential destructive index (PDI), which is proportional to the square of the greatest sustained wind speed, to represent the typhoon strength for destruction. He demonstrated that the typhoon strength for the northern Pacific has increased over the past 30 years. Webster et al. (2005) indicated that, although the total number of typhoons in the world has not changed in the past 30 years, the global typhoon strength exhibits increasing trends consistent with those of the SST. This effect is particularly notable in the strongest category-4 and category-5 typhoons. Wu et al. (2005) analyzed the best track from 1965 to 2003 and showed that the two prevailing typhoon tracks in the western North Pacific shifted substantially westward; thus, the Taiwan waters experienced increasing typhoon influences. This shift might increase the probability of extreme wave events occurring. Kossin et al. (2007) performed statistical analysis based on observation data from the National Climatic Data Center and the National Hurricane Research Center, examining inter-annual changes in hurricane PDI worldwide. The results showed a trend of significant increases in typhoon PDI in the northwest Pacific throughout the previous 20 years, which is consistent with the results of Emanuel (2005).

The correlation analysis between the western North Pacific SST anomaly and the occurrence of summer ELSE is illustrated in Fig. 14a. The corresponding correlation coefficient was 0.47, suggesting a moderate correlation. Because the number of summer ELWEs could be used as an indicator of the variation of recent typhoon strength around Taiwan, these results suggest that, from the beginning of the 1980s, typhoons have played an increasingly dominant role in Taiwan waters.

#### 4.2 Frequency analysis of ELWEs in the Northwest Pacific

We further extended the analysis of ELWEs to the spatial domain, including the northwest Pacific and the Luzon Strait. In this example, the threshold significant wave height was set to 5.0 m and the threshold duration was 4 h. The contour maps illustrating the occurrence of summer and winter ELWEs are shown in Figs. 15 and 16, respectively. In each figure, panels a and b represent the occurrence averaged over two durations (i.e., the former: 1948–1982; the latter: 1983–2008). The differences between panel a and panel b were obtained by subtracting the occurrence of the former period from that of the latter period, as shown in panel c. Comparison between Figs. 15 and 16 shows that the occurrence of ELWEs was three times lower in summer than winter. Regarding the area in

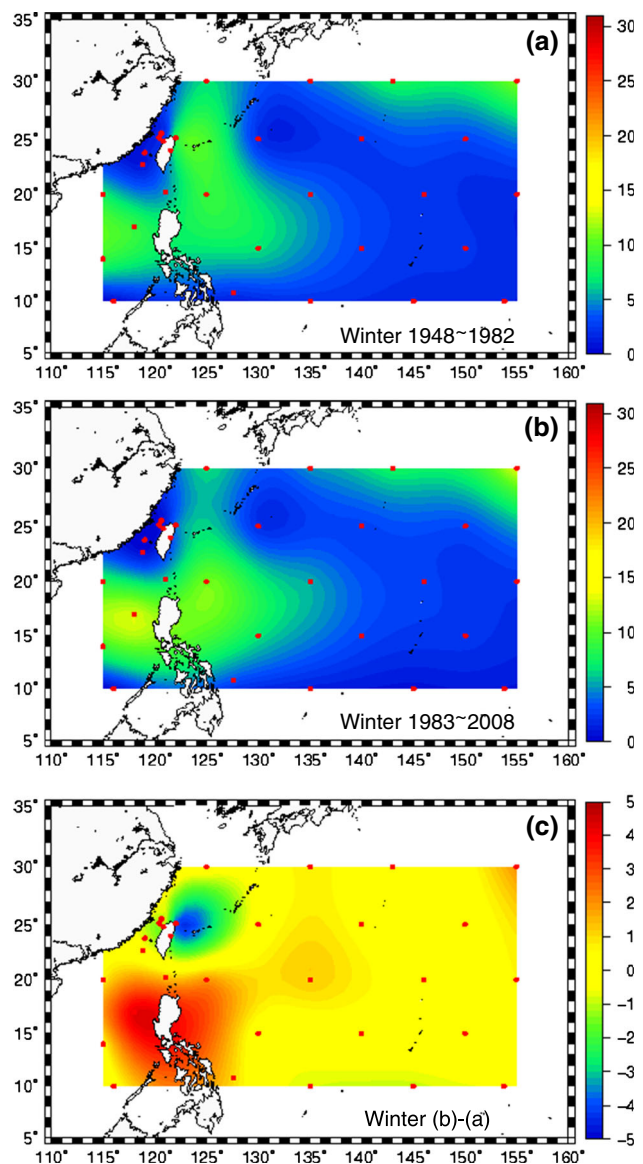


**Fig. 16** The spatial distribution of the annual extreme wave events in winter: **a** average from 1947 to 1982, **b** average from 1983 to 2008. The difference is illustrated in **(c)**

which frequent ELWEs occur near Taiwan waters, substantial discrepancies existed between the summer and winter seasons. Qualitatively, the summer ELWEs occurred mostly in the region northeast of Taiwan and along the East China Sea shelf break to Okinawa, whereas the winter ELWEs frequently occurred in the areas that cover the zonal stripe of 7°–20°N and the meridional stripe of 122°–128°E near Luzon. According to Fig. 15c, a slightly increasing trend of summer ELWEs could be identified east and south of Taiwan, especially in the northern South China Sea west of Luzon. In contrast to the summer ELWEs, there was an obvious temporal variation in the spatial patterns of the occurrence of winter ELWEs. As shown in Fig. 16c, the occurrence number of winter ELWEs exhibits

a rapid decrease in the northeastern coast of Taiwan. This result is consistent with the decreasing trend in the frequency of winter ELWEs at the Longdong coast.

## 5 Conclusions

In this study, we discussed the variability of wave climate in Taiwan waters with respect to different temporal scale oscillations and trends. It can be concluded that, over the last six decades, the wave climate in Taiwan waters has undergone considerable changes. Regarding the temporal variance of wave characteristics, the waters around Taiwan exhibit strong oscillations in the seasonal scale. January is the most energetic period of the year. Around the northeast coasts around Taiwan, for example, the average wave heights in winter were 2.2 times higher than were those in summer. The wave energy and wave steepness were 3.3 and 1.2 times higher in winter than in summer, respectively. The ratio between the potential wave energy in winter and summer seasons varies according to the location and might reach 3.7 on the western coast.

Concerning inter-annual oscillation, El Niño and La Niña are also associated with the wave climate oscillations. Regarding wave energy strength, wave energy increases in La Niña years and decreases in El Niño years. If wave height calculations are performed for engineering design using either El Niño years or La Niña years, the difference could be as much as one multiple. These inter-annual oscillations could negatively influence the wave energy conversion capacity factor and reduce the benefit:cost ratio. The wave climate also exhibits a decadal long-period oscillation. Correlation analysis was performed for the decadal wave climate oscillation and PDO, revealing a moderate correlation between them.

Concerning the long-term trend, in the past 60 years, significant wave heights have trended downward each year at an average of 0.31 cm/year. Winter season wave height and wave energy have been dropping gradually at the rate 0.86 cm/year, which is related to the weakening of the winter monsoons. The wave height and wave energy in the summer months have been increasing at the rate of 0.5 cm/year.

This study examined the probability of occurrence for various ELWEs in the waters around Taiwan. The results showed that extreme events in the past 60 years were concentrated between 1967 and 1974 and 2000 and 2008. Extreme events occurring in the latter period involved larger waves for longer periods of time. Regarding the probability of ELWEs in the waters around Taiwan, the occurrence frequency has been decreasing in winter and increasing in summer. Concerning the spatial variation, extreme events in the winter season have significantly

decreased near the northeast corner of Taiwan; extreme events have moved southward. The number of extreme events occurring in the South China Sea and in the Luzon Strait have increased. These phenomena may be related to the weakening of the winter monsoons. ELWEs occurring in the summer season were caused entirely by typhoons. The frequency of extreme events occurring in the summer season has increased slightly. Following the 1980s, the number of ELWEs caused by typhoons exceeded those caused by winter monsoons.

## References

- Allan JC, Komar PD (2000) Are ocean wave heights increasing in the eastern North Pacific? *Eos Trans AGU* 47:561–567
- Allan JC, Komar PD (2001) Wave climate change and coastal erosion in the US Pacific Northwest. In: Proceedings: WAVES2001 conference held September 2–6, 2001 in San Francisco. American Society of Civil Engineer
- Alves JHGM, Banner ML (2003) Performance of a saturated-based dissipation-rate source term in modeling the fetch-limited evolution of wind waves. *J Phys Oceanogr* 33:1274–1298
- Barnett DN, Brown SJ, Murphy JM, Sexton DMH, Webb MJ (2006) Quantifying uncertainty in changes in extreme event frequency in response to doubled CO<sub>2</sub> using a large ensemble of GCM simulations. *Clim Dyn* 26(5):489–511
- Bjerknes J (1969) Atmospheric teleconnections from the equatorial Pacific. *Mon Weather Rev* 97:163–172
- Booij N, Holthuijsen LH, Ris RC (1996) The SWAN wave model for shallow water. In: Proceedings of 25th Int. Conf. Coastal Engineering, vol 1, Orlando, USA, pp 668–676
- Booij N, Ris RC, Holthuijsen LH (1999) A third-generation wave model for coastal regions 1. Model description and validation. *J Geophys Res* 104:7649–7666
- Bromirski PD, Cayan DR, Flick RE (2005) Wave spectral energy variability in the northeast Pacific. *J Geophys Res* 110:C03005
- Chawla A, Spindler DM, Tolman HL (2012) Validation of a thirty year wave hindcast using the climate forecast system reanalysis winds. *Ocean Model.* doi:[10.1016/j.ocemod.2012.07.005](https://doi.org/10.1016/j.ocemod.2012.07.005)
- Chen W, Graf HF, Huang R (2001) The interannual variability of East Asian winter monsoon and its relation to the summer monsoon. *Adv Atmos Sci* 17(1):48–60
- Chiou MD, Winter C, Kao CC (2007) Storm surge hindcast in the north sea. In: The 9th Asian Symposium on Visualization, Hong Kong, June 4–8
- Collins M, An S-I, Cai W, Ganachaud A, Guilyardi E, Jin F-F, Jochum M, Lengaigne M, Power S, Timmermann A, Vecchi G, Wittenberg A (2010) The impact of global warming on the tropical Pacific Ocean and El Niño. *Nat Geosci* 3(6):391–397
- Deser C, Blackmon ML (1993) Surface climate variations over the North Atlantic Ocean during winter: 1900–1989. *J Clim* 6:1743–1753
- Dodet G, Bertin X, Taborda R (2010) Wave climate variability in the North-East Atlantic Ocean over the last six decades. *Ocean Model* 31:120–131
- Easterling DR (2000) Climate extremes observation modeling and impact. *Science* 289:2068
- Emanuel KA (2001) The contribution of tropical cyclones to the oceans' meridional heat transport. *J Geophys Res* 106:14771–14781
- Emanuel KA (2005) Increasing destructiveness of tropical cyclones over the past 30 years. *Nature* 436:686–688
- Flandrin P, Rilling G, Goncalves P (2004) Empirical mode decomposition as a filter bank. *Signal Proc Lett IEEE* 11:112–114
- Glantz MH (2001) Current of Change: impacts of El Niño and La Niña on climate and society, 2nd edn. Cambridge University Press, Cambridge
- Gong D-Y, Ho C-H (2002) Shift in the summer rainfall over the Yangtze River valley in the late 1970s. *Geophys Res Lett* 29:1436
- Gong DY, Wang SW (1999) Long-term variability of the Siberian high and the possible influence of global warming. *Acta Geogr Sin* 54(2):125–133 (in Chinese)
- Grabemann I, Weisse R (2008) Climate change impact on extreme wave conditions in the North Sea: an ensemble study. *Ocean Dyn* 58:122–129
- Graham NE, Diaz HF (2001) Evidence for intensification of north Pacific winter cyclones since 1948. *Bull Am Met Soc* 82:1869–1893
- Gulev SK, Grigorieva V (2006) Variability of the winter wind waves and swell in the North Atlantic and North Pacific as revealed by the voluntary observing ship data. *Int J Climatol* 19:5667–5685
- Harrison GP, Wallace AR (2005) Sensitivity of wave energy to climate change. *IEEE Trans Energy Convers* 20:870–877
- Hirsch RM, Slack JR (1984) A non-parametric trend test for seasonal data with serial dependence. *Water Resour Res* 20(6):727–732
- Hirsch RM, Slack JR, Smith RA (1982) Techniques of trend analysis for monthly quality data. *Water Resour Res* 18(1):107–121
- Huang NE, Coauthors (1998) The empirical mode decomposition and the Hilbert spectrum for nonlinear and non-stationary time series analysis. *Proc R Soc Lond B* 454A:903–995
- Huang NE, Wu Z (2008) A review on Hilbert-Huang transform: method and its applications to geophysical studies. *Rev Geophys* 46:RG2006. doi:[10.1029/2007RG000228](https://doi.org/10.1029/2007RG000228)
- Jan Sen, Wang J, Chern C-S, Chao S-Y (2002) Seasonal variation of the circulation in the Taiwan Strait. *J Mar Syst* 35:249–268
- Kang LH, Chen W, Wei K (2006) The interdecadal variation of winter temperature in China and its relation to the anomalies in atmospheric general circulation (in Chinese). *Clim Environ Res* 11:303–309
- Kitoh A (1988) Correlation between the surface air temperature over Japan and the global sea surface temperature. *J Meteor Soc Jpn* 66:967–986
- Komen GJ, Hasselmann S, Hasselmann K (1984) On the existence of a fully developed wind-sea spectrum. *J Phys Oceanogr* 14:1271–1285
- Kossin JP, Knapp KR, Vimont DJ, Murnane RJ (2007) A globally consistent reanalysis of hurricane trends. *Geophys Res Lett* 34:L04815. doi:[10.1029/2006GL028836](https://doi.org/10.1029/2006GL028836)
- Large WG, Pond S (1981) Open ocean-momentum flux measurements in moderate to strong winds. *J Phys Oceanogr* 11:324–336
- Lee Y-A (2002) A T-EOF based prediction method. *J Clim* 15:226–234
- Lee B-C, Chien H, Cheng H-Y, Chiou M-D (2010) Evaluation of operational wave forecasts for northeastern coast of Taiwan. *Terr Atmos Ocean Sci* 21(1):195–210. doi:[10.3319/TAO.2009.06.03.02](https://doi.org/10.3319/TAO.2009.06.03.02)
- Lins HF, Slack JR (1999) Streamflow trends in the United States. *Geophys Res Lett* 26:227–230
- Mantua NJ, Hare SR (2002) The Pacific decadal oscillation. *J Oceanogr* 58:35–44
- McPhaden MJ (1999) Genesis and evolution of the 1997–1998 El Niño. *Science* 283:950–954
- McPhaden MJ, Picaut J (1990) El Niño-Southern oscillation displacements of the western equatorial Pacific warm pool. *Science* 250:1385–1388

- Menéndez M, Méndez FJ, Losada IJ, Graham NE (2008) Variability of extreme wave heights in the northeast Pacific Ocean based on buoy measurements. *Geophys Res Lett* 35:L22607. doi:[10.1029/2008GL035394](https://doi.org/10.1029/2008GL035394)
- Mori N, Yasuda T, Mase H, Tom T, Oku Y (2010) Projection of extreme wave climate change under global warming. *Hydrol Res Lett* 4:15–19
- Nicholls N (2008) Recent trends in the seasonal and temporal behaviour of the El Niño Southern Oscillation. *Geophys Res Lett* 35:L19703
- Parmesan C, Yohe G (2003) A globally coherent fingerprint of climate. *Integr Nat* 421:37–42
- Ringuet S, Mackenzie FT (2005) Controls of nutrient and phytoplankton dynamics during normal flow and storm runoff conditions, southern Kaneohe Bay, Hawaii. *Estuar Coasts* 28(3):327–337
- Ruggiero P, Komar PD, Jonathan CA (2010) Increasing wave heights and extreme value projections: the wave climate of the US Pacific Northwest. *Coastal Eng* 57(5):539
- Sasaki W, Hibiya T (2007) Interannual variability and predictability of summertime significant wave heights in the western North Pacific. *J Oceanogr* 63:203–213
- Sasaki W, Iwasaki SI, Matsuura T, Lisuka S, Watabe I (2005) Changes in wave climate off Hiratsuka, Japan, as affected by storm activity over the western North Pacific. *J Geophys Res* 110(C09008):13. doi:[10.1029/2004JC002730](https://doi.org/10.1029/2004JC002730)
- Slott JM, Murray AB, Ashton AD, Crowley TJ (2006) Coastline responses to changing storm patterns. *Geophys Res Lett* 33:L18404. doi:[10.1029/2006GL027445](https://doi.org/10.1029/2006GL027445)
- Snyder R, Dobson FW, Elliott JA, Long RB (1981) Array measurements of atmospheric pressure fluctuations above surface gravity waves. *J Fluid Mech* 102:1–59
- Sterl A, Komen GJ, Cotton PD (1998) Fifteen years of global wave hindcasts using winds from the European Centre for medium-range weather forecast reanalysis: validating the reanalyzed winds and assessing the wave climate. *J Geophys Res* 103:5477–5492
- Swail VR, Cox AT (2000) On the use of NCEP/NCAR reanalysis surface marine wind fields for a long-term North Atlantic wave hindcast. *J Atmos Oceanic Technol* 17:532–544
- Vanem Erik, Natvig B, Huseby AB (2012) Modelling the effect of climate change on the wave climate of the World's oceans. *Ocean Sci J* 47:123–145
- Wang XL, Swail VR (2001) Changes of extreme wave heights in north hemisphere oceans and related atmospheric circulation regimes. *J Clim* 14:2204–2221
- Wang B, Wu RG, Fu XH (2000) Pacific-East Asian teleconnection: how does ENSO affect East Asian climate? *J Clim* 13:1517–1536
- Wang L, Chen W, Huang R (2008) Interdecadal modulation of PDO on the impact of ENSO on the East Asian winter monsoon. *Geophys Res Lett* 35:L20702. doi:[10.1029/2008GL035287](https://doi.org/10.1029/2008GL035287)
- Webster PJ, Holland GJ, Curry JA, Chang H-R (2005) Changes in tropical cyclone number, duration and intensity in a warming environment. *Science* 309:1844–1846
- Woolf DK, PG Challenor, PD Cotton (2002) Variability and predictability of the North Atlantic wave climate. *J Geophys Res* 107. doi:[10.1029/2001JC001124](https://doi.org/10.1029/2001JC001124)
- Wu ZH, Huang NE (2009) Ensemble empirical mode decomposition: a noise-assisted data analysis method. *Adv Adapt Data Anal* 1:1–41
- Wu L, Wang B, Geng S (2005) Growing typhoon influence on East Asia. *Geophys Res Lett* 32:L18703. doi:[10.1029/2005GL022937](https://doi.org/10.1029/2005GL022937)
- Yamaguchi M, Hatada Y (2003) Estimation of wave climate and its long-term variability around the coasts of Korea. In: Proceedings of 13th ISOPE conference, Hawaii
- Yeh S-W, Kug J-S, Dewitte B, Kwon M-H, Kirtman BP, Jin F-F (2009) El Niño in a changing climate. *Nature* 461(7263): 511–514
- Zhang Y, Sperber KR, Boyle JS (1997) Climatology and interannual variation of the East Asian winter monsoon: results from the 1979–95 NCEP/NCAR reanalysis. *Mon Weather Rev* 125:2605–2619
- Zhang K, Douglas BC, Leatherman SP (2004) Global warming and coastal erosion. *Clim Change* 64:41–58
- Zhang J, Yan R, Gao RX (2009) Ensemble empirical mode decomposition for machine health diagnosis. *Key Eng Mater* 413–414:167–174